Research Square

Preprints are preliminary reports that have not undergone peer review.
They should not be considered conclusive, used to inform clinical practice,
or referenced by the media as validated information.

Bryophyte-Inspired Gas Diffusion Electrode Reveals Unex-pected CO Formation Kinetics under Dilute CO2

Yinlong Zhu

zhuyl1989@nuaa.edu.cn

Nanjing University of Aeronautics and Astronautics https://orcid.org/0000-0002-9207-2452

Mingxu Sun

Nanjing University of Aeronautics and Astronautics

Yuyao Wang

Nanjing University of Aeronautics and Astronautics

Zheng Tang

Nanjing University of Aeronautics and Astronautics

Article

Keywords:

Posted Date: August 21st, 2026

DOI: https://doi.org/10.21203/rs.3.rs-10716107/v1

License: This work is licensed under a Creative Commons Attribution 4.0 International License.
Read Full License

Additional Declarations: There is **NO** Competing Interest.

Bryophyte-Inspired Gas Diffusion Electrode Reveals Unexpected CO Formation Kinetics under Dilute CO_2

Mingxu Sun,* Yuyao Wang, Zheng Tang and Yinlong Zhu*

[1]State Key Laboratory of Mechanics and Control for Mechanical Structures, Key Laboratory for Intelligent Nano Materials and Devices of the Ministry of Education, Institute for Frontier Science, Nanjing University of Aeronautics and Astronautics, Nanjing, 210016, China

*Corresponding author Email: mingxu.sun@nuaa.edu.cn; zhuyl1989@nuaa.edu.cn

Direct electrolysis of dilute CO_2 streams could circumvent the energy demand associated with CO_2 capture and purification but is limited by inefficient CO_2 transport and the poorly understood kinetic consequences of CO_2 dilution. Here, we develop a bryophyte-inspired gas diffusion electrode that integrates ordered Cu nanowire transport channels with a locally engineered Zn(100)-rich catalyst to simultaneously regulate macroscopic CO_2 transport and microscopic catalytic interfaces. Using this platform, we uncover an unexpected non-monotonic dependence of CO formation on CO_2 concentration, with CO formation reaching its fastest kinetics at only 10% CO_2 rather than under pure CO_2. This counterintuitive behavior enables a single-pass conversion efficiency of 92% while allowing direct tuning of industrially relevant syngas compositions. Isotope-labeling experiments together with in situ spectroscopy reveal two-hydrogen-bonded interfacial water as the reactive hydrogen source for *COOH formation, establishing interfacial water as the missing kinetic link between CO_2 transport and catalytic CO formation under dilute feeds.

Electrochemical CO_2 reduction (CO_2RR) provides a promising route for converting CO_2 into value-added chemicals and fuels using renewable electricity. Among the possible products, carbon monoxide (CO) is particularly attractive because it serves both as a key component of syngas and as an essential feedstock for established chemical processes such as Fischer–Tropsch synthesis and methanol production.[1-3] Considerable progress has been made in CO electrolysis, with many catalyst systems achieving high selectivity at industrially relevant current densities.[4-7]

Despite these advances, nearly all high-performance CO_2 electrolyzers operate with purified CO_2 feeds. In contrast, practical emission sources, including flue gases from cement, steel, and power plants, typically contain only 2–30 vol% CO_2 diluted primarily by N_2.[8-11] Consequently, energy-intensive capture and purification steps are generally required before electrolysis, substantially increasing both the economic and environmental costs of carbon utilization.[12, 13] In addition, many of the most efficient CO selective catalysts rely on noble metals or sophisticated single-atom architectures,[14-16] raising concerns regarding scalability and large-term deployment.

Direct electrolysis of dilute CO_2 streams therefore represents an attractive alternative.[17, 18] However, low concentration CO_2 electrolysis is not simply a feed dilution problem.[19, 20] Introducing large amounts of N_2 changes the transport environment within porous electrodes.[21] Besides the reduced CO_2 partial pressure, intermolecular diffusion between CO_2 and N_2 and Knudsen diffusion inside tortuous pores can substantially hinder CO_2 delivery to catalytic interfaces.[22] More importantly, how diluted feeds influence the reaction pathway and kinetics of CO_2 reduction remains largely unexplored.

Inspired by the rhizoid system of bryophytes, which facilitates nutrient uptake and transport under nutrient-limited conditions,[23, 24] we envisioned that ordered transport channels could alleviate these diffusion limitations and improve the utilization of dilute CO_2 feeds (Fig. 1a). Compared with conventional carbon gas diffusion layers (GDLs) composed of disordered pores, aligned nanowire architectures may provide more direct gas transport pathways and larger gas–solid interfacial areas. Furthermore, replacing chemically inert carbon frameworks with Cu surfaces may strengthen CO_2 adsorption and promote directional molecular transport. Beyond overcoming mass transport limitations, catalyst design remains equally critical for efficient CO production from dilute CO_2 feeds. Earth-abundant Zn has emerged as a promising alternative to noble-metal or single-atom catalysts because of its low cost and intrinsic preference toward CO formation. However, its catalytic performance is highly sensitive to surface structure and the local reaction environment,[25-27] and effective strategies to simultaneously regulate these factors remain limited.

Here, we report a bryophyte-inspired gas diffusion electrode that integrates these two design principles through macroscopic regulation of CO_2 transport and microscopic engineering of catalytic interfaces. Ordered Cu nanowire channels accelerate CO_2 transport under dilute feeds, while locally alkaline electrodeposition tailors the Zn catalyst toward preferential Zn(100) facet exposure and exceptional CO_2RR performance over a wide pH range. Using this platform, we uncover an unexpected non-monotonic dependence of CO formation kinetics on CO_2 concentration, where the fastest CO production occurs at only 10% CO_2. This unique kinetic behavior enables a single pass conversion efficiency (SPCE) of up to 92% under dilute feeds and can be exploited to directly tune industrially relevant syngas compositions. Combined isotope-labeling and in situ spectroscopic studies further reveal that two-hydrogen-bonded interfacial water actively participates in *COOH formation, identifying reactive interfacial water as a previously overlooked factor governing CO_2RR under dilute feed conditions.

Results and Discussion

Bryophyte-Inspired Cu Nanowire Channels Enable Directional CO_2 Transport

To address the severe transport limitations associated with dilute CO_2 electrolysis, we first constructed a bryophyte-inspired gas diffusion layer featuring aligned Cu nanowire channels, in contrast to the tortuous pore network of conventional carbon-based GDLs (Fig. 1a). The two architectures were designed with identical geometric dimensions and porosity, allowing the influence of transport pathway morphology to be isolated. COMSOL simulations were subsequently performed to compare CO_2 diffusion within the disordered porous network and ordered nanowire channels under both pure CO_2 and 15% CO_2/85% N_2 feeds (Supplementary Fig. 1, see Supplementary Note 1 for COMSOL simulations details). Representative concentration profiles after 2 μs diffusion are shown in Fig. 1b. Compared with the disordered porous structure, the ordered nanowire channels exhibited substantially more direct diffusion trajectories, as evidenced by the nearly linear transport pathways throughout the GDL thickness (Fig. 1b, Supplementary Figs. 2 and 3). In contrast, CO_2 transport within the conventional porous architecture followed highly tortuous routes, leading to frequent changes in diffusion direction and prolonged transport distances (Fig. 1b, Supplementary Figs. 4 and 5). Quantitative analysis of the outlet CO_2 concentration further confirmed the transport advantage of the ordered architecture (Fig. 1c, Supplementary Fig. 6). After 2 μs diffusion, the outlet CO_2 concentration reached 1.13 mM for the ordered nanowire channels under pure CO_2, significantly higher than that of the disordered porous structure (0.42 mM). A similar trend was observed under the dilute feed condition, where the ordered channels maintained approximately twofold higher outlet CO_2 concentrations than the disordered pores.

To experimentally validate the simulation results, CO_2 diffusion measurements were performed using differential electrochemical mass spectrometry (DEMS), where the temporal evolution of the CO_2 signal was used to estimate the apparent diffusion rate through different GDLs (Supplementary Fig. 7, and Table 1, see Supplementary Note 2 for details). As summarized in Fig. 1d, excellent agreement was observed between simulations and experiments under pure CO_2 conditions (Supplementary Figs. 8 and 9). The ordered Cu nanowire GDL exhibited approximately 2.4–2.8 times higher apparent diffusion rates than the conventional carbon GDL, confirming the effectiveness of ordered transport channels in promoting gas transport. Interestingly, a markedly different behavior emerged under dilute feed conditions (Fig. 1d). Although simulations predicted a substantial decrease in diffusion rates owing to the additional diffusion resistance introduced by N_2, the experimentally measured transport rates were significantly higher than expected for both architectures. This discrepancy became particularly pronounced for the ordered Cu nanowire GDL, whose experimentally measured diffusion rate exceeded that of the conventional carbon GDL operating under pure CO_2. These observations suggest that transport enhancement in dilute CO_2 feeds cannot be fully explained by macroscopic channel geometry alone and that additional molecular level interactions may contribute to the observed diffusion behavior.

To uncover the origin of this unexpected transport enhancement, molecular dynamics simulations were performed in confined carbon and Cu nanochannels with identical dimensions of 50 nm × 1.5 nm. (Supplementary Figs. 10–15, see Supplementary Notes 3–6 for details). As shown in Fig. 1e, CO_2 molecules displayed markedly different diffusion behaviors on the two channel surfaces. Within the carbon channel, CO_2 molecules were distributed throughout the channel volume with relatively disordered trajectories. In contrast, diffusion in the Cu channel became highly localized near the channel walls, forming a distinct wall-guided transport mode. Such

preferential migration along the Cu surface effectively reduced random molecular motion within the channel interior and generated a more ordered diffusion pathway. This behavior becomes particularly important under dilute feed conditions, where intermolecular collisions between CO_2 and N_2 substantially increase diffusion resistance. To quantify the origin of this wall-guided diffusion behavior, the interaction strength between CO_2 and the channel surfaces was further evaluated. As shown in Fig. 1f, CO_2 exhibits a substantially stronger affinity toward Cu (−7.72 kcal mol^{-1}) than carbon (−2.36 kcal mol^{-1}). The enhanced CO_2–Cu interaction promotes preferential adsorption and migration along the channel walls, thereby providing a molecular-level explanation for the superior transport performance observed experimentally.

Taken together, the combined simulation and experimental results demonstrate that the superior transport capability of the bryophyte-inspired GDL originates not only from the reduction of geometric tortuosity by ordered nanowire channels but also from Cu-mediated molecular guidance that becomes increasingly important under dilute CO_2 conditions.

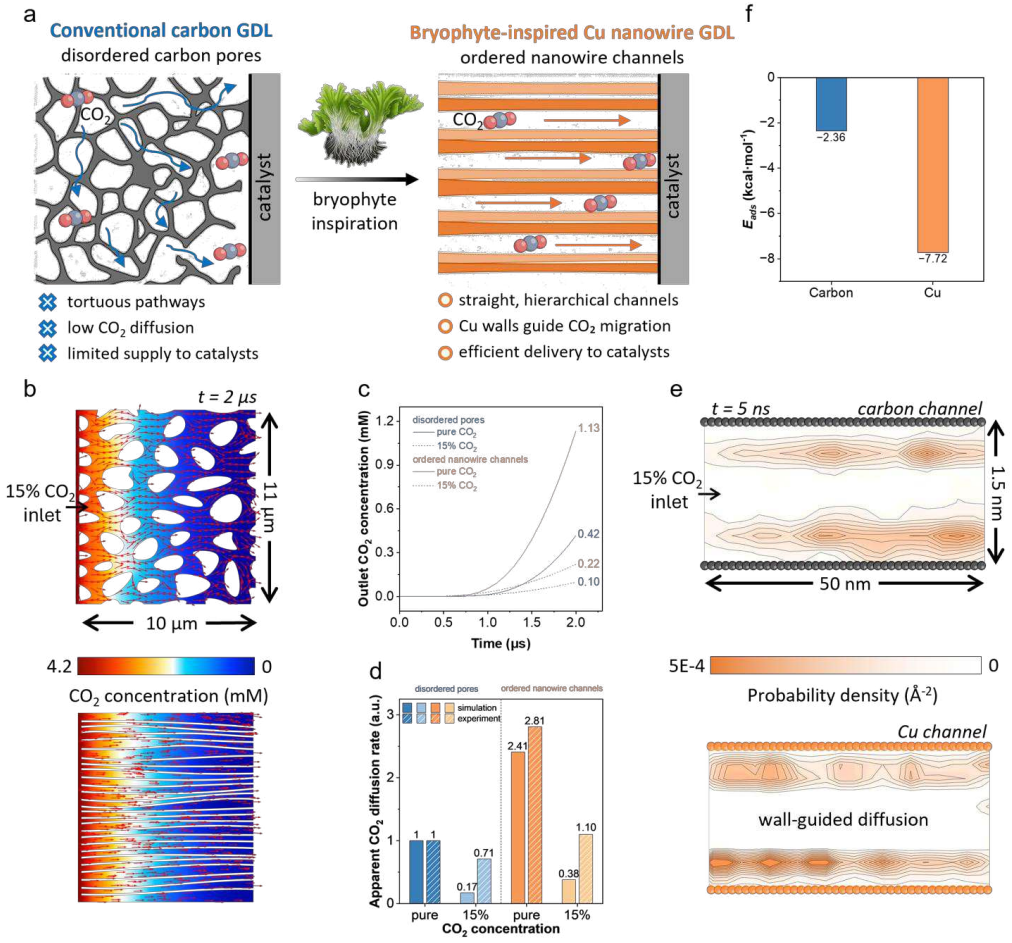


Fig. 1 Bryophyte-inspired gas diffusion layer for directional CO_2 transport. (a) Design concept of the bryophyte-inspired gas diffusion layer featuring aligned Cu nanowire channels for directional CO_2 transport. (b) COMSOL simulated CO_2 concentration distributions in disordered pores and ordered nanowire channels under 15% CO_2 feed at 2 μs diffusion. Upper, disordered pores. Lower, ordered Cu nanowire channels. (c) Simulated outlet CO_2 concentration profiles as a function of diffusion time. (d) Simulated and experimentally measured CO_2 transport rates under different feed concentrations. (e) Molecular dynamics simulations of CO_2 diffusion in confined channels after 5 ns diffusion. Upper, carbon channel. Lower, Cu channel. Preferential CO_2 transport along the Cu channel walls results in a more ordered diffusion pathway. (f) Adsorption energies of CO_2 on carbon and Cu surfaces.

Local Alkaline Microenvironment Directs Zn Electrodeposition

Following the establishment of efficient CO_2 transport pathways, we next sought to optimize the catalytic interface for selective CO production. Zn was selected as the catalytic component because of its earth abundance, low cost, and intrinsic preference for CO formation. [25, 28] However, Zn catalysts typically suffer from competing hydrogen evolution, which limits their CO selectivity under practical operating conditions.[29, 30] Previous studies have shown that locally alkaline environments can effectively suppress hydrogen evolution by reducing proton availability near the catalyst surface.[31, 32] We therefore hypothesized that the electrochemical growth of Zn on the bryophyte-inspired Cu nanowire framework could simultaneously construct the catalyst and generate a locally alkaline microenvironment favorable for CO_2-to-CO conversion (Fig. 2a).

To verify this hypothesis, an operando rotating ring-disk electrode (RRDE) configuration was employed to monitor local pH evolution during Zn electrodeposition (Supplementary Figs. 16–18, see Supplementary Notes 7 and 8 for details).[33, 34] In this setup, the conventional disk electrode was replaced by the Cu nanowire substrate, while an IrO_x-modified ring electrode was used as a pH-sensitive probe. During the first cathodic sweep, the local pH increased from approximately 5.9 to 9.3 as the cathodic current increased, indicating substantial OH^- accumulation arising from water reduction. Notably, although the subsequent anodic sweep temporarily decreased the local pH, the pH recovered to approximately 9.3 when the current returned to near zero values, suggesting that the alkaline microenvironment generated during Zn deposition remained partially preserved at the electrode surface (Fig. 2b). More importantly, consecutive potential cycling resulted in a progressive enhancement of the local alkalinity. During the second cycle, the local pH approached ~15 under strongly cathodic polarization and stabilized at approximately 12.5 after the cycle was completed. A similar behavior was observed in the third cycle, indicating that the alkaline microenvironment had reached a stable state and could no longer be significantly enhanced through additional cycling. These observations demonstrate that Zn electrodeposition on the Cu nanowire framework is capable of generating and retaining a highly alkaline interfacial environment, with the attainable local pH governed by the magnitude of the deposition current.

Based on these findings, two Zn electrodes with distinct local pH characteristics were intentionally prepared by varying the deposition current density while maintaining the same total transferred charge. Specifically, deposition at -1 mA cm^{-2} for 9000 s produced the Zn-shell electrode, whereas deposition at -100 mA cm^{-2} for 90 s yielded the Zn-leaf electrode (see Methods for details). Operando pH monitoring during deposition revealed markedly different alkaline environments for the two electrodes (Fig. 2c). Zn-shell maintained a local pH of approximately 9.3 throughout deposition, whereas Zn-leaf generated an extremely alkaline environment with local pH values ranging from 13.8 to 15. The resulting alkaline microenvironments remained stable after electrodeposition (Fig. 2d). Zn-shell retained a mildly alkaline surface with a local pH of approximately 9.3, whereas Zn-leaf maintained a strongly alkaline interface with a local pH of approximately 12.5. These results demonstrate that the electrodeposition strategy enables precise regulation of the local chemical environment surrounding Zn catalysts, providing a well-defined platform for subsequently investigating the relationship between interfacial alkalinity, catalyst structure, and CO_2RR performance.

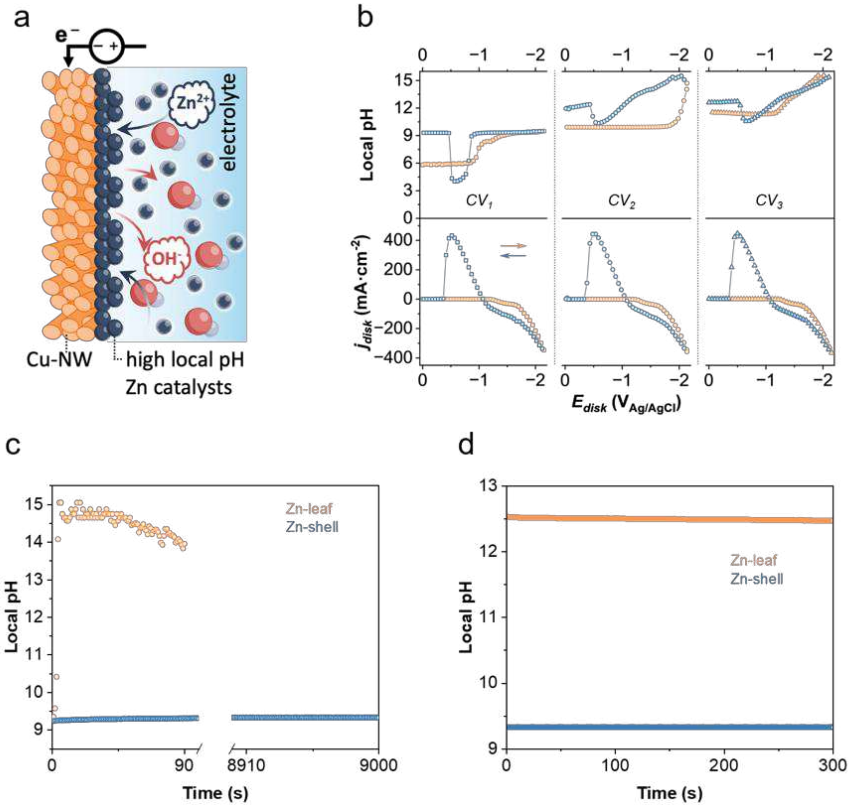


Fig. 2 Construction of a locally alkaline microenvironment on Zn electrodes. (a) Schematic illustration of the regulation of the local alkaline microenvironment on Zn electrodes. (b) Correlation between the cyclic voltammetry (CV) current density of the Cu-NW disk electrode (bottom) and the corresponding local pH near the disk electrode surface (top). CV_1, CV_2, and CV_3 represent three consecutive CV cycles recorded on the disk electrode. (c) Local pH response during Zn electrodeposition for Zn-leaf at −100 mA cm^{-2} for 90 s and for Zn-shell at −1 mA cm^{-2} for 9000 s under identical transferred charge conditions. (d) Local pH response as a function of resting time after electrodeposition for Zn-leaf at −100 mA cm^{-2} for 90 s and for Zn-shell at −1 mA cm^{-2} for 9000 s, demonstrating the enhanced stability of the locally generated alkaline microenvironment for Zn-leaf (pH ≈ 12.5) compared with Zn-shell (pH ≈ 9.3).

Local Alkalinity Induces Preferential Zn(100) Facets for Efficient CO Electroproduction

Having established the feasibility of constructing locally alkaline Zn surfaces, we next prepared two model electrodes, namely Zn-shell (pH ≈ 9.3) and Zn-leaf (pH ≈ 12.5), to elucidate the influence of the alkaline microenvironment on catalyst structure and CO_2RR performance. Porous Cu foil was first employed as the gas diffusion substrate (Fig. 3a), upon which a dense Cu nanowire GDL (Cu-NW GDL) was grown through the in situ oxidation–reduction strategy developed in our previous work (Fig. 3b, see Supplementary Note 9 for details).[35] Subsequent electrochemical Zn deposition under low (–1 mA cm^{-2}) and high (–100 mA cm^{-2}) current densities generated Zn-shell and Zn-leaf, respectively (see Methods for details). The resulting electrodes exhibit markedly different growth behaviors depending on the local pH during deposition. SEM images reveal distinct growth behaviors of Zn under different local pH conditions. Zn-shell preserves the original Cu nanowire morphology and forms a conformal shell surrounding the nanowires (Supplementary Fig. 19), whereas Zn-leaf exhibits leaf-like hierarchical structures assembled from stacked hexagonal nanosheets (Figs. 3c, d). Notably, the overall morphology of Zn-leaf closely resembles the rhizoid–leaf architecture of bryophyte, consisting of Cu nanowire "rhizoids" supporting Zn "leaves".

To enable stable operation as gas diffusion electrodes, both catalysts were further modified with a small amount of Poly[4,5-difluoro-2,2-bis(trifluoromethyl)-1,3-dioxole-co-1,3-dioxane-2-(difluoromethylene)-4,5,5,6,6-pentafluoro-4-(trifluoromethyl)] (denoted as PFD, see Methods for electrode hydrophobization details). The resulting electrodes exhibit superhydrophobic characteristics with initial water contact angles (CAs) of approximately 155° (Fig. 3c inset and Supplementary Fig. 20), ensuring stable gas–liquid separation and efficient three-phase interfaces during CO_2 electrolysis. The uniform distribution of PFD on both electrodes was further verified by XPS and elemental mapping (Supplementary Figs. 21 and 22). To gain insight into the origin of the distinct morphologies and microenvironments generated under different deposition conditions, XPS measurements were first conducted on the as-prepared electrodes prior to PFD modification. The Zn 2p spectra of both Zn-leaf and Zn-shell closely resemble that of metallic Zn foil, with characteristic Zn 2p3/2 and Zn 2p1/2 peaks located at 1021.7 and 1044.7 eV, respectively (Supplementary Fig. 23),[36] indicating that metallic Zn constitutes the dominant surface species. Interestingly, the O 1s spectra reveal substantial differences between the two electrodes. Compared with Zn-shell, Zn-leaf exhibits a pronounced hydroxyl-related component centered at 531.3 eV, indicating the presence of abundant surface hydroxyl species (Supplementary Fig. 24).[37] This observation directly supports our design principle that intense local OH^- generation during electrodeposition can be incorporated into the catalyst surface, thereby producing a stable locally alkaline microenvironment. The Cu 2p spectra further show the complete disappearance of Cu signals after Zn deposition (Supplementary Fig. 25), confirming that the catalytic surface is fully covered by Zn and excluding any contribution from exposed Cu sites during CO_2RR.

Given the distinct local chemical environments identified above, we next investigated whether the alkaline growth conditions also influence the crystallization behavior of Zn. Unlike Zn-leaf, which exhibits diffraction peaks well matching those of metallic Zn foil, Zn-shell shows almost no discernible Zn reflections in the XRD pattern (Fig. 3e), suggesting the formation of a largely amorphous Zn phase under mild deposition conditions. More importantly, Zn-leaf displays an unusually intensified Zn(100) reflection compared with Zn foil, implying a preferential exposure of the Zn(100) facet. To directly verify this hypothesis, HAADF-STEM analysis was performed. Large domains of highly ordered hexagonal atomic arrangements are observed throughout the Zn-leaf nanosheets (Fig. 3f). The measured lattice spacing of 2.31 Å can be assigned to the Zn(100) plane (Fig. 3g), confirming the dominant exposure of Zn(100) facets. Quantitative analysis of the XRD peak areas further demonstrates that all other Zn facets are substantially suppressed relative to Zn foil, with their relative fractions decreasing to only 31.3–79.6% of the Zn(100)-normalized reference value (Fig. 3h, Supplementary Figs. 26–28, and Table 2). These results collectively indicate that the locally alkaline growth environment selectively promotes the formation of Zn(100)-dominated catalysts. Such a pronounced facet redistribution suggests that the catalytic behavior of Zn-leaf may differ fundamentally from that of conventional Zn catalysts. To understand the catalytic significance of the preferentially exposed Zn(100) facets, DFT calculations were performed on the six experimentally identified Zn surfaces (see Supplementary Note 10, and Table 3–8 for computational details). Among all investigated facets, Zn(100) exhibits the most favorable adsorption of the $*CO_2$ intermediate, with an adsorption energy of only 0.11 eV (Fig. 3i). More importantly, the rate-determining step on Zn(100), corresponding to CO desorption, requires only 0.43 eV, significantly lower than those on the other facets. These results indicate that Zn(100) simultaneously facilitates the initial activation of CO_2 and lowers the overall reaction barrier for CO formation, rationalizing the exceptional CO_2RR activity of Zn-leaf. Theoretical predictions therefore suggest that Zn-leaf should exhibit superior intrinsic CO_2RR activity. ECSA measurements exclude surface area effects as the origin of the

superior activity of Zn-leaf (see Supplementary Fig. 29, and Note 11 for details of ECSA analysis), as Zn-leaf possesses a substantially smaller electrochemically active surface area than Zn-shell. In contrast, DRT analysis reveals significantly reduced resistive contributions associated with charge transfer, interfacial processes, and mass transport on Zn-leaf, suggesting more favorable reaction kinetics (see Supplementary Fig. 30 for details of DRT analysis).

Motivated by these structural and kinetic advantages, we next evaluated the CO_2RR performance of Zn-leaf and Zn-shell in a near neutral KCl electrolyte to minimize additional influences arising from electrolyte alkalinity or Zn passivation. Zn-leaf exhibits remarkable CO selectivity over the entire industrially relevant current density (j) range from −0.3 to −1.2 A cm^{-2} (Fig. 3j), maintaining Faradic efficiency of CO (FE_{CO}) values exceeding 80%. In contrast, Zn-shell shows acceptable selectivity only at −0.3 A cm^{-2} and suffers a continuous decline in FE_{CO} as the j increases. Consequently, the maximum partial current density for CO (j_{CO}) production on Zn-leaf approaches −1 A cm^{-2}, more than twice that achieved by Zn-shell. Collectively, these results demonstrate that coupling a locally alkaline microenvironment with preferential Zn(100) facet exposure fundamentally alters the catalytic behavior of Zn, enabling efficient CO production at industrial j using a fully earth-abundant electrode.

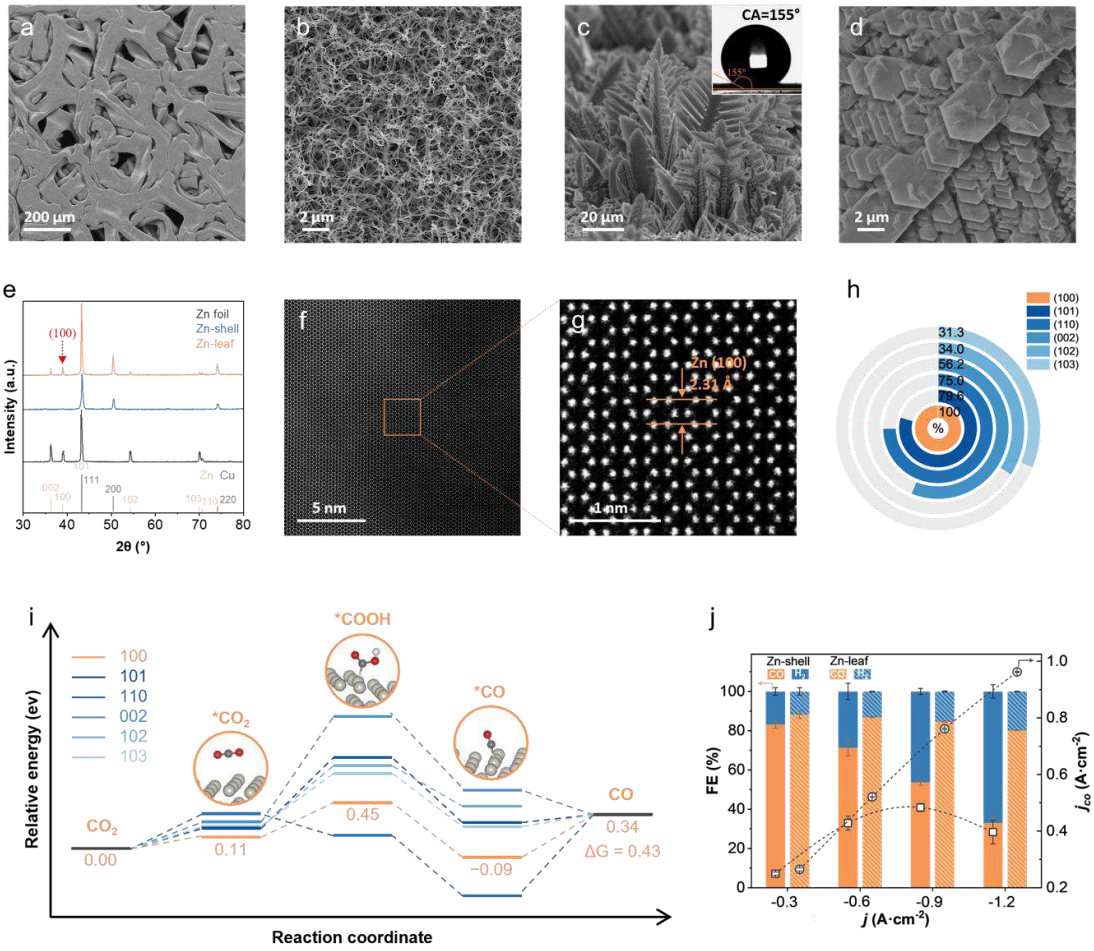


Fig. 3 Preferential formation of Zn(100)-dominated catalysts under locally alkaline conditions. (a) SEM image of porous Cu foil. (b) SEM image of Cu-NW. (c, d) SEM images of Zn-leaf. The inset in (c) shows the initial contact angle of Zn-leaf. (e) XRD patterns of Zn foil, Zn-shell, and Zn-leaf. (f, g) HAADF-STEM images of Zn-leaf, where (g) is a magnified view of the selected region in (f). (h) Relative facet intensity ratios of Zn-leaf calculated using the Zn (100) reflection as the reference. (i) DFT-calculated reaction pathways for CO formation on different Zn facets. The inset shows the representative adsorption configurations of reaction intermediates on the Zn (100) facet. (j) Comparison of the CO_2RR performance between Zn-shell and Zn-leaf.

Broad-pH and High-Rate CO_2-to-CO Electrolysis on Zn-leaf

Having identified Zn-leaf as the most promising catalyst architecture, we next optimized its preparation conditions and systematically evaluated its CO_2RR performance under pure CO_2 feeds. To optimize the catalyst loading, Zn electrodeposition was conducted at a fixed j of −100 mA cm^{-2} while varying the deposition time from 18 to 108 s (see Methods for details). SEM images reveal the gradual evolution of Zn from isolated nuclei into densely packed leaf-like nanosheets with increasing deposition time (Supplementary Fig. 31). Correspondingly, all electrodes exhibit FE_{CO} values above 80% at relatively low j ($\leq$ −0.6 A cm^{-2}) (Fig. 4a, Supplementary Fig. 32). However, electrodes prepared for 18–54 s suffer from a pronounced decline in CO selectivity at higher j, suggesting insufficient catalyst loading to sustain rapid CO_2 conversion. In contrast, Zn-leaf electrodes deposited for 72–108 s maintain high CO selectivity over the entire j range investigated. Considering both activity and performance stability, the electrode prepared for 90 s was selected for subsequent studies.

Having established the optimized electrode structure, we then examined the influence of electrolyte pH on CO_2RR performance. Because Zn catalysts are generally susceptible to corrosion under acidic conditions and passivation under alkaline environments,[38] achieving efficient CO_2 electrolysis over a broad pH range remains challenging. We therefore evaluated CO_2RR performance of Zn-leaf in representative acidic (pH 2), neutral (pH 7), and alkaline (pH 14) electrolytes (Supplementary Note 12 and 13). Remarkably, Zn-leaf exhibits outstanding CO selectivity under all three conditions (Fig. 4b, Supplementary Tables 9–11). Although alkaline electrolytes deliver the highest FE_{CO} values (~95%), the performance differences among the three pH conditions remain surprisingly small, with FE_{CO} variations generally below 10% at identical j. In particular, nearly identical CO selectivities are observed both at low current densities (−0.1 to −0.3 A cm^{-2}) and at ultrahigh current densities ($\geq$ −2.7 A cm^{-2}). This result indicates that Zn-leaf is largely insensitive to the external electrolyte environment and can sustain efficient CO production across an exceptionally broad pH window. The universal pH adaptability of Zn-leaf is further reflected in its exceptionally high reaction rates. Under all pH conditions, j_{CO} production approaches −1.8 A cm^{-2}, corresponding to CO formation rates of nearly 9.4 μmol s^{-1} cm^{-2} (Fig. 4c, Supplementary Tables 9–11). Similar trends are also observed in $KHCO_3$ electrolytes (Supplementary Figs 33 and 34, and Table 12), although a moderate decrease in performance is observed at high j, likely due to additional transport limitations imposed by (bi)carbonate species.[39, 40]

The corresponding j_{CO} as a function of potential further demonstrate the remarkable operational flexibility of Zn-leaf (Fig. 4d). Efficient CO production can be sustained over an exceptionally wide potential window ranging from approximately −0.53 to −3.71 V vs RHE. Such broad operational tolerance highlights the practical potential of Zn-leaf for industrial CO_2 electrolysis under diverse operating conditions. To evaluate long-term durability, we further implemented an electrolyte self-refreshing system that continuously neutralizes accumulated (bi)carbonate species by automated acid addition (Supplementary Fig. 35, see Supplementary Note 14 for details). Under industrially relevant conditions (−200 mA cm^{-2}, pH ≈ 6), Zn-leaf maintains stable operation for over 100 h without electrolyte replacement or operational interruption, exhibiting less than 10% decay in FE_{CO} (Supplementary Fig. 36). This level of continuous operation compares favorably with previously reported Zn-based flow-cell systems. Finally, we benchmarked Zn-leaf against state-of-the-art Zn catalysts using multiple metrics, including FE_{CO}, j_{CO}, ΔE, ΔpH, and FR_{CO} (Fig. 4e, Supplementary Table 13).[25, 41-44] Zn-leaf simultaneously delivers high selectivity, industrial-level current densities, broad pH adaptability, wide operating potentials,

and rapid CO production rates, collectively surpassing the performance envelope of previously reported Zn-based CO_2-to-CO electrocatalysts.

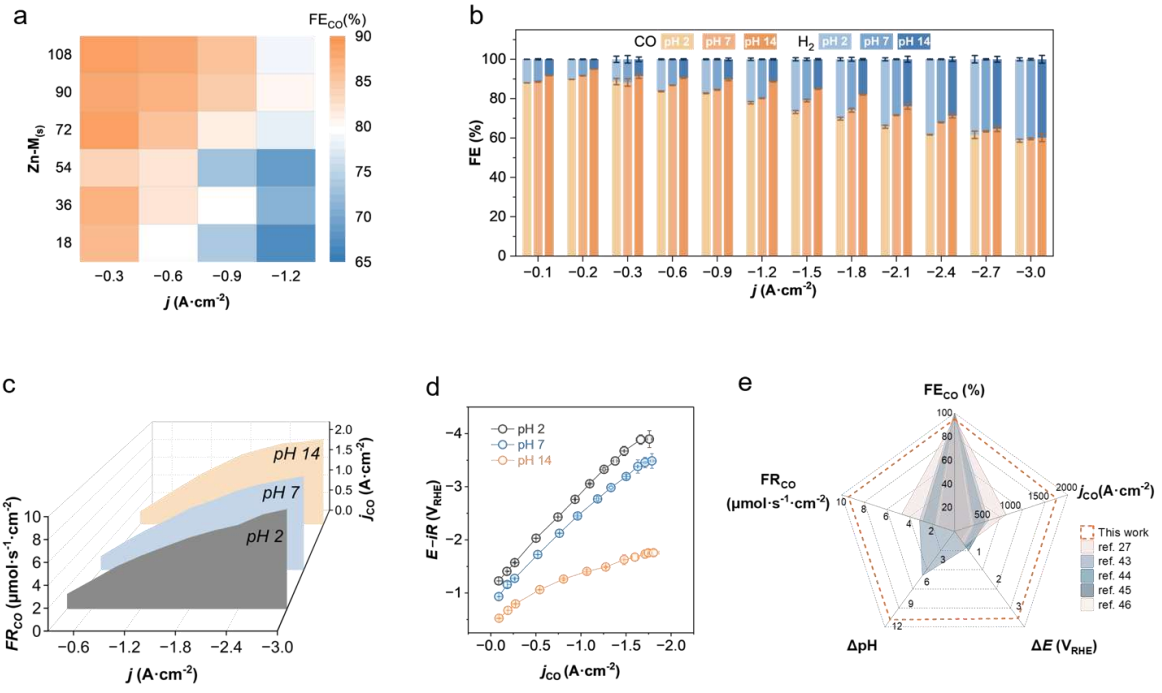


Fig. 4 pH universal CO_2 electroreduction on Zn-leaf under pure CO_2. (a) FE_{CO} as a function of j prepared with different electrodeposition times ranging from 18 to 108 s. (b) FE_{CO} and FE_{H_2} as a function of j measured at pH 2, 7, and 14. (c) FR_{CO} and j_{CO} as a function of j measured at pH 2, 7, and 14. (d) j_{CO} as a function of the iR-corrected potential versus RHE measured at pH 2, 7, and 14. (e) Comparison of FE_{CO}, j_{CO}, ΔE, ΔpH, and FR_{CO} with those of previously reported state-of-the-art Zn-based CO_2RR catalysts. (b) and (d) error bars indicate s.d. (n = 3 replicates).

Diluted CO_2 Induces Unusual Reaction Kinetics for CO Electroproduction

Having established the excellent CO_2RR performance of Zn-leaf under pure CO_2 conditions, we next extended our investigation to diluted CO_2 feeds that more closely resemble practical industrial exhaust streams. Industrial flue gases typically contain only 2–30% CO_2, with N_2 being the predominant balance gas. Direct electrochemical utilization of such diluted CO_2 streams would eliminate the energy-intensive purification and concentration processes currently required for conventional CO_2 electrolysis. Although industrial exhaust gases may also contain minor components such as O_2, SO_x, and NO_x,[45-47] these species introduce additional competitive reactions and catalyst poisoning effects that are beyond the scope of the present study. Therefore, CO_2/N_2 mixtures were selected herein to isolate the intrinsic influence of CO_2 concentration on electroreduction behavior (Fig. 5a).

Polarization measurements under CO_2 concentrations ranging from 2% to 30% reveal an unexpected and non-monotonic dependence of electrochemical activity on CO_2 concentration (Fig. 5b). Surprisingly, the 10% CO_2 feed delivers the highest j at a given potential, outperforming both more concentrated and more diluted feeds. This observation immediately suggests that the reaction kinetics are not solely governed by CO_2 availability and that an additional concentration dependent factor may be involved. To determine whether the anomalous polarization behavior simply originates from changes in product selectivity, we systematically evaluated the CO_2RR performances under different CO_2 concentrations (Fig. 5c, Supplementary Fig. 37). Interestingly, for CO_2 concentrations between 10% and 30%, FE_{CO} does not decrease with increasing j but

instead gradually increases. Moreover, the FE_{CO} difference between the 10% and 30% systems remains below 10% throughout the investigated *j* range. These observations indicate that the substantially different polarization behaviors cannot be solely attributed to a shift from CO production toward HER, implying that genuine kinetic differences exist among the various CO_2 concentrations.

To gain further insight into the origin of these kinetic differences, Tafel analyses were performed (Fig. 5d, Supplementary Tables 14–18). Most CO_2 concentrations exhibit two or even three distinct Tafel regions, suggesting that the reaction mechanism evolves with increasing reaction rate and changing reactant availability. In sharp contrast, the 10% CO_2 system displays a single Tafel slope of only 193 mV dec^{-1} across the entire investigated current density range, indicating a remarkably stable and accelerated reaction pathway. Considering that CO formation on Zn mainly proceeds through proton-coupled elementary steps, we hypothesized that the altered CO_2/H ratio under diluted CO_2 conditions may change the participation of hydrogen-containing intermediates and consequently modify the reaction kinetics. To test this hypothesis, isotope experiments were conducted by replacing H_2O with D_2O (Fig. 5e). At −160 mA cm^{-2} under 10% CO_2, the operating potential dramatically shifts from −1.39 to −2.16 V versus SHE upon isotopic substitution, corresponding to an increase of approximately 0.77 V. Such a pronounced kinetic isotope effect clearly demonstrates that proton transfer plays a critical role in determining the reaction kinetics under diluted CO_2 conditions. Interestingly, although D_2O substantially suppresses the reaction kinetics, FE_{CO} simultaneously increases from 61.3% to 86.7%, suggesting that proton participation acts as a double-edged sword by accelerating both CO_2RR and the competing HER process. This result further implies that a delicate balance exists between reaction kinetics and product selectivity through the participation of hydrogen-containing intermediates.

The discovery of exceptionally fast CO formation kinetics under 10% CO_2 prompted us to consider whether this kinetic advantage could be exploited to improve carbon utilization efficiency. SPCE represents one of the most challenging metrics in CO_2 electrolysis because maximizing carbon utilization becomes increasingly difficult as the feed concentration decreases. Achieving high SPCE under a 10% CO_2 feed requires converting nearly every available CO_2 molecule before it is lost through parasitic carbonate formation. To suppress carbonate accumulation, an acidic electrolyte (pH 2) was employed. Remarkably, Zn-leaf achieves an ultrahigh SPCE of 92% under only 10% CO_2 while sacrificing less than 15% of FE_{CO} (Fig. 5f, Supplementary Fig. 38). Considering that most previous studies require pure CO_2 feeds to reach comparable carbon utilization, the present result highlights the unique advantage of the accelerated kinetics under diluted CO_2 conditions.

Beyond carbon utilization, the concentration dependent kinetics also offer an opportunity for product engineering. Although the annual production of pure CO is only approximately 1 million tons,[48] the global syngas market exceeds 250 million tons per year,[49] highlighting the much broader industrial demand for tunable CO/H_2 mixtures. Because CO and H_2 are both valuable constituents of syngas, we envisioned that the balance between CO_2RR and HER could be manipulated simply by tuning the CO_2 feed concentration and reaction rate. By varying the CO_2 concentration from 10% to 30% and the *j* from −0.3 to −1.5 A cm^{-2}, a wide CO/H_2 ratio ranging from 8:2 to 1:9 can be continuously achieved under industrially relevant current densities (Fig. 5g, Supplementary Fig. S39, and Table 19). Such broad tunability eliminates the need for downstream gas ratio adjustment and provides a versatile route toward on demand syngas production.[50, 51] Finally, considering that approximately 15% CO_2 is widely employed to simulate industrial flue gas compositions, long-term electrolysis was performed under 15% CO_2 at −200 mA cm^{-2} (Fig. 5h). Zn-leaf maintains a

stable FE_{CO} of approximately 70% over 20 h of continuous operation using the automatic electrolyte-refresh system developed above. Post electrolysis characterization reveals that the overall leaf-like architecture remains largely preserved, whereas the surface features become blurred and the contact angle decreases from 155° to approximately 120° (Supplementary Fig. 40), suggesting that gradual deterioration of surface hydrophobicity is primarily responsible for the eventual performance decay.

Collectively, these results demonstrate that diluted CO_2 feeds do not necessarily deteriorate CO_2 electroreduction. Instead, an intermediate CO_2 concentration unexpectedly optimizes proton-assisted reaction kinetics, enabling simultaneously high carbon utilization and flexible syngas production. These findings provide both fundamental insights into diluted CO_2 electroreduction and practical opportunities for the direct valorization of industrial exhaust gases.

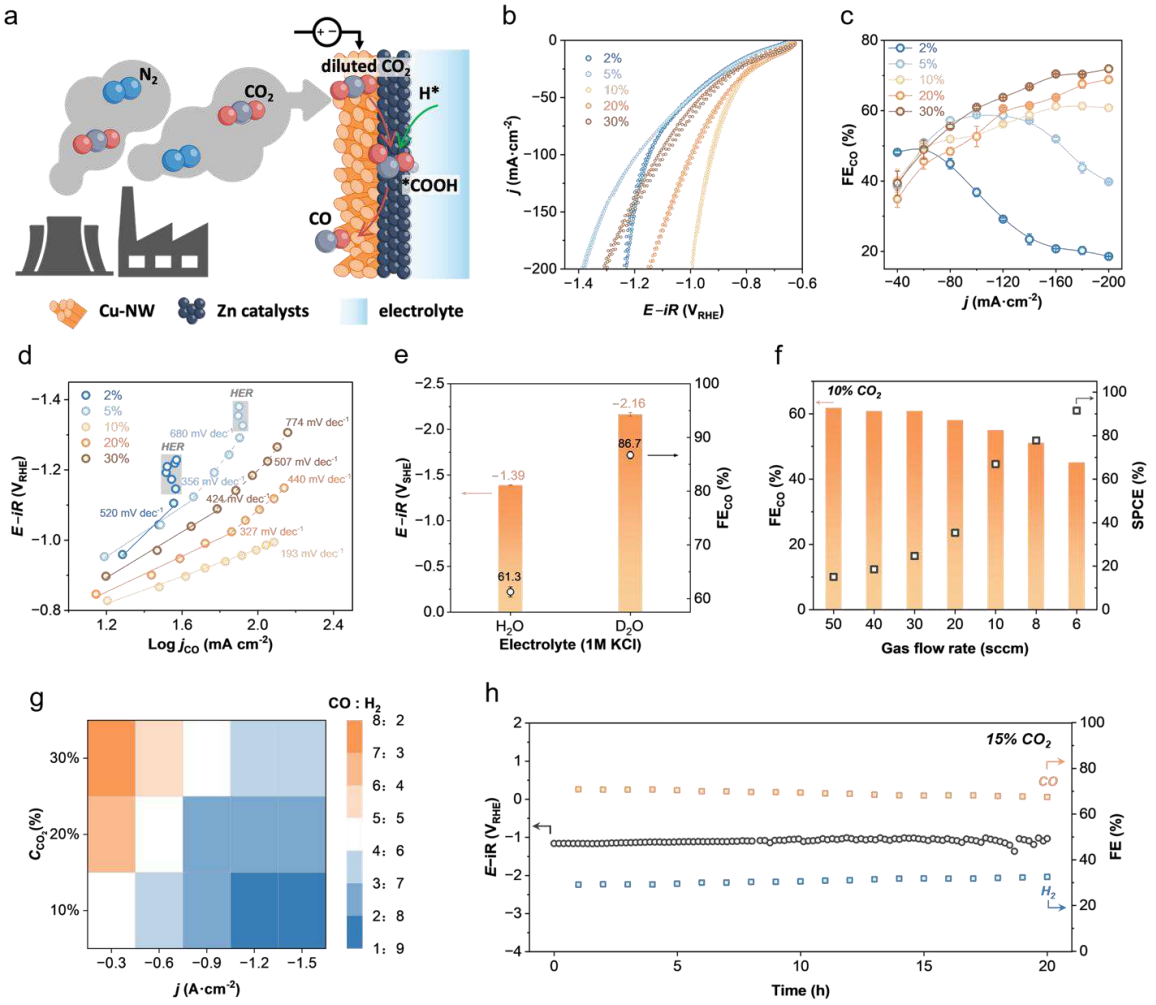


Fig. 5 Accelerated CO_2 electroreduction under diluted CO_2 conditions. (a) Schematic illustration of the accelerated *COOH formation promoted by *H under diluted CO_2 conditions to facilitate CO_2RR kinetics. (b) Polarization curves of Zn-leaf measured under different CO_2 concentrations (2%, 5%, 10%, 20%, and 30%). (c) FE_{CO} as a function of j under different CO_2 concentrations (2%, 5%, 10%, 20%, and 30%). (d) Tafel slopes for CO formation under different CO_2 concentrations (2%, 5%, 10%, 20%, and 30%). (e) Comparison of the FE_{CO} and the applied potential versus SHE for CO_2RR using H_2O and D_2O as the electrolyte solvent under 10% CO_2 at a j of −160 mA cm^{-2}. (f) FE_{CO} and the corresponding SPCE as a function of CO_2 gas flow rate under 10% CO_2 at a j of −160 mA cm^{-2}. (g) Ratio of the FE_{CO} and FE_{H_2} as a function of j under CO_2 concentrations ranging from 10% to 30% at j from −0.3 to −1.5 A cm^{-2}. (h) Long-term stability evaluation of Zn-leaf under 15% CO_2 at a j of −200 mA cm^{-2}. (c) and (e) error bars indicate s.d. (n = 3 replicates).

Reactive Interfacial Water Accelerates Diluted CO_2 Electroreduction

The unusual kinetic enhancement observed under 10% CO_2 suggests that the concentration effect cannot be solely interpreted by changes in carbon availability. Instead, the pronounced isotope effect and the unique Tafel behavior imply that proton transfer originating from interfacial water plays a crucial role in regulating the CO_2 reduction kinetics (Figs. 5d, e). We therefore sought to identify the active water species and clarify its mechanistic contribution to the formation of the key *COOH intermediate (Fig. 6a).

To this end, in situ DEMS was first employed to monitor the real-time formation rates of CO and H_2 in 0.1 M $KHCO_3$ electrolyte (see Supplementary Note 15 for details). Consistent with the flow cell results shown in Fig. 5, the 10% CO_2 system exhibits a substantially larger current response than pure CO_2 over the investigated potential range (Fig. 6b), confirming that the accelerated kinetics under diluted CO_2 is intrinsic and can also be reproduced under dissolved CO_2 conditions. More importantly, the CO signal recorded by DEMS reveals a clear crossover behavior (Fig. 6c). Between −0.1 and −0.4 V versus RHE, the CO generation rate under 10% CO_2 exceeds that obtained under pure CO_2, despite the considerably lower CO_2 concentration. In contrast, the H_2 signal remains negligible in this potential region (Fig. 6d), indicating that HER contributes minimally and that the observed enhancement predominantly originates from CO_2 reduction itself. This potential range therefore provides an ideal window for mechanistic investigations.

To probe the origin of this kinetic enhancement, in situ ATR-FTIR was subsequently performed (Supplementary Figs. 41 and 42, see Supplementary Note 16 for details). Under both pure CO_2 and 10% CO_2 conditions, two characteristic bands can be clearly identified (Figs. 6e, f): the ν(C–O) vibration of adsorbed *COOH (~1370 cm^{-1}) and the δ(H–O–H) bending mode of interfacial water (~1660 cm^{-1}).[52] Remarkably, quantitative integration of these bands reveals that the evolution of the *COOH signal closely tracks that of interfacial water over the potential range from −0.1 to −0.4 V (Fig. 6g). Such a strong correlation suggests that the formation of *COOH is intimately coupled with the dissociation of interfacial water, supporting a PCET process in which hydrogen derived from water participates directly in the hydrogenation of CO_2.

The next question is therefore which type of interfacial water is responsible for this process. According to previous studies, interfacial water can generally be classified into four-hydrogen-bonded (4-HB), two-hydrogen-bonded (2-HB), and free H_2O configurations according to their hydrogen-bonding environments.[53-56] To identify the reactive species, the broad O–H stretching region was deconvoluted following literature procedures (Figs. 6h, i, Supplementary Table 21). Interestingly, comparison of the relative peak contributions demonstrates that only the 2-HB H_2O exhibits an evolution trend that closely mirrors the variation of the *COOH signal (Fig. 6j, Supplementary Tables 22 and 23). Neither the strongly hydrogen-bonded 4-HB H_2O nor free H_2O shows such correspondence (Supplementary Figs. 43 and 44, and Tables 24 and 25). These results identify 2-HB H_2O as the active interfacial water species participating in the rate-determining proton-transfer process.

Based on these observations, we propose that the accelerated kinetics under diluted CO_2 conditions originates from the enhanced participation of reactive 2-HB H_2O molecules in the PCET step (Fig. 6a). Compared with the highly ordered and strongly hydrogen-bonded 4-HB network, the weaker hydrogen-bond interactions in 2-HB H_2O render its O–H bonds more labile, facilitating proton relay toward adsorbed CO_2 species and lowering the kinetic barrier for *COOH formation.

Taken together, these results reveal an unexpected mechanism governing diluted CO_2 electroreduction. The reaction kinetics are dictated not only by the availability of carbon feedstock but also by the structure and reactivity of the interfacial hydrogen-bond network. By tuning the balance between CO_2 supply and reactive interfacial water, diluted CO_2 conditions can unexpectedly promote rather than suppress CO_2 activation. This finding establishes interfacial water engineering as a previously underappreciated strategy for regulating CO_2 electroreduction under realistic low concentration carbon sources. More broadly, these results suggest that lowering the CO_2 concentration does not necessarily penalize CO_2 electroreduction. Instead, it can fundamentally reconstruct the interfacial hydrogen-bond network and unlock new reaction pathways that are inaccessible under conventional pure CO_2 conditions. This work therefore introduces diluted CO_2 as not merely a challenging feedstock, but as a new reaction regime for manipulating interfacial water chemistry and electrocatalytic kinetics.

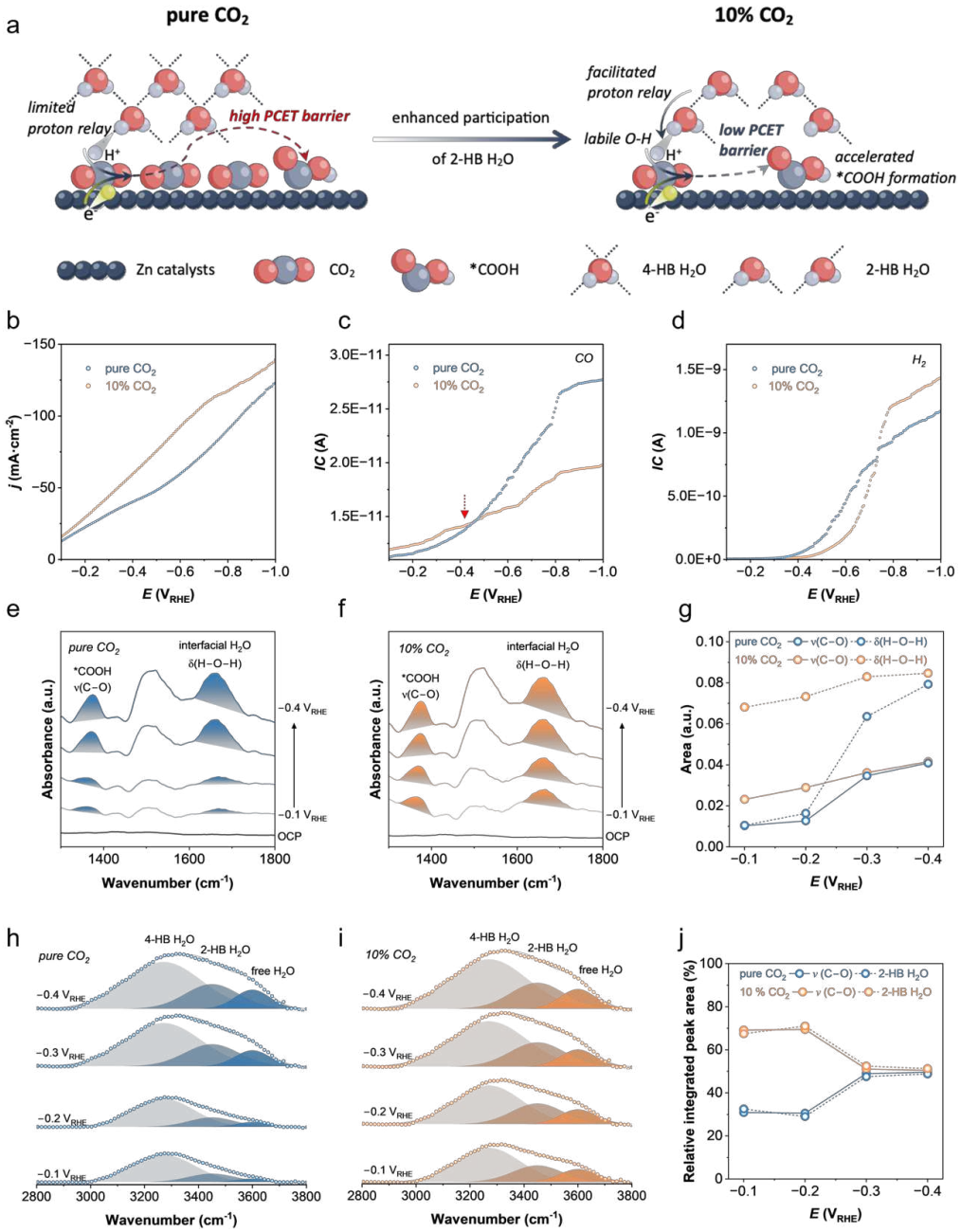


Fig. 6 Interfacial water regulates *COOH formation under diluted CO_2. (a) Schematic illustration of the proposed role of interfacial water configurations in regulating the PCET process for *COOH formation under pure CO_2 and diluted CO_2 atmospheres. The scheme highlights the different participation of HB H_2O species during CO_2 activation. (b) LSV recorded during in situ DEMS measurements under pure CO_2 and 10% CO_2 atmospheres in 0.1 M $KHCO_3$ electrolyte. (c, d) In situ DEMS analysis of (b) CO and (c) H_2 ionic currents as a function of potential versus RHE under pure CO_2 and 10% CO_2 atmospheres in 0.1 M $KHCO_3$ electrolyte. The applied potential range was from −0.1 to −1.0 V versus RHE. (e, f) In situ ATR-FTIR spectra collected under pure (e) CO_2 and (f) 10% CO_2 atmospheres at potentials ranging from OCP to −0.4 V versus RHE, showing the evolution of the ν(C–O) vibration of *COOH related intermediates and the δ(H–O–H) bending mode of interfacial H_2O. The shaded areas indicate the integrated peak regions used for quantitative analysis. (g) Comparison between the integrated peak areas of the ν(C–O) vibration associated with *COOH related intermediates and the δ(H–O–H) bending mode of interfacial H_2O obtained from in situ ATR-FTIR spectra under pure CO_2 and 10% CO_2 atmospheres at potentials ranging from −0.1 to −0.4 V versus RHE. (h, i) Deconvolution analysis of the O–H stretching region of interfacial water obtained from the in situ ATR-FTIR spectra under pure (h) CO_2 and (i) 10% CO_2 atmospheres, showing the evolution of 4-HB H_2O, 2-HB H_2O, and free H_2O species. (j) Comparison between the relative integrated peak area contributions of *COOH related intermediates and 2-HB H_2O species under pure CO_2 and 10% CO_2 atmospheres derived from the in situ ATR-FTIR spectra.

Conclusions

In summary, we developed a bryophyte-inspired Zn-leaf electrode that achieves efficient CO_2-to-CO electrolysis over a wide range of pH values and CO_2 concentrations. Beyond the performance advances, we reveal an unexpected kinetic feature of diluted CO_2 electroreduction. Decreasing the CO_2 concentration does not necessarily suppress CO_2RR but can instead accelerate CO formation kinetics. Mechanistic investigations identify reactive 2-HB H_2O as the origin of this behavior, where enhanced participation of 2-HB H_2O facilitates PCET and promotes *COOH formation. These findings establish a direct connection between reactant concentration, interfacial water structure, and electrocatalytic kinetics, suggesting that diluted CO_2 represents not merely a challenging feedstock but a new opportunity for manipulating interfacial chemistry and designing electrochemical systems for realistic carbon resources.

Methods

Chemicals and materials Hydrochloric acid (HCl, 36 wt%, AR), acetone (99.5%, AR), ethanol (99.7%, AR), ammonium sulfate ($(NH_4)_2SO_4$, 99.0%, AR), zinc sulfate heptahydrate ($ZnSO_4·7H_2O$, 99.5%, AR), potassium hydroxide (KOH, ACS, 99.5%), and potassium bicarbonate ($KHCO_3$, AR, 99.5%) were purchased from Shanghai Aladdin Biochemical Technology Co., Ltd. Ammonia solution ($NH_3·H_2O$, 25–28%, AR), sulfuric acid (H_2SO_4, 98.0%, AR), oxalic acid dihydrate ($C_2H_2O_4·2H_2O$, ≥99.5%, AR), hydrogen peroxide (H_2O_2, 30 wt%), and potassium carbonate (K_2CO_3, AR) were obtained from Sinopharm Chemical Reagent Co., Ltd. Deuterium oxide (D_2O, 99.8%) was purchased from Energy Chemical Technology. Iridium (IV) chloride ($IrCl_4$, ≥99.9%) was purchased from Shanghai Macklin Biochemical Co., Ltd. Poly[4,5-difluoro-2,2-bis(trifluoromethyl)-1,3-dioxole-co-1,3-dioxane-2-(difluoromethylene)-4,5,5,6,6-pentafluoro-4-(trifluoromethyl)] (denoted as PFD) and fluorinated electronic liquid (FC-770) were purchased from Shanghai Puchun Industrial Co., Ltd. All chemicals were used as received without further purification. Fumasep FAA-3-PK-130 membranes, Nafion 117 membranes, and gas diffusion layers (SGL-28 BC) were purchased from Suzhou Sinero Technology Co., Ltd. High-purity Zn foil (purity ≥ 99.99%, thickness = 0.1 mm) was supplied by Kesirui New Materials Co., Ltd. A customized porous Cu foil was used as the gas diffusion electrode substrate. High-purity N_2 (99.999%) and CO_2 (99.999%) gases were purchased from Nanjing Tianhong Gas Co., Ltd. Deionized water (18.25 MΩ cm) was used for the preparation of all aqueous solutions.

Characterization X-ray diffraction (XRD) patterns were collected using a Bruker D2 PHASER diffractometer operated at 30 kV with Cu Kα radiation (λ = 1.54184 Å). Scanning electron microscopy (SEM) images were acquired using a TESCAN LYRA3 GM microscope. Transmission electron microscopy (TEM) and elemental mapping analyses were performed using

a Talos F200X G2 microscope. High-angle annular dark-field scanning transmission electron microscopy (HAADF-STEM) images were obtained using a Thermo Fisher Scientific Spectra 300 (S)TEM. X-ray photoelectron spectroscopy (XPS) measurements were conducted using an ESCALAB Xi+ spectrometer equipped with an Al Kα X-ray source, with a spot size of 650 μm, a pass energy of 20 eV, and an energy step size of 0.05 eV. Rotating ring-disk electrode (RRDE) measurements were carried out using a Pine Research Instrumentation system. Static water contact angles were measured at ambient temperature using a Solon Tech SL200B digital goniometer with a 10 μL water droplet. Differential electrochemical mass spectrometry (DEMS, QMG 100, Linglu Instrument Equipment Co., Ltd.,) equipped with dual Faraday cup/SEM detectors was employed for operando gaseous product analysis during electrochemical reactions over a mass range of 1–100 amu. Attenuated total reflection Fourier-transform infrared (ATR-FTIR) spectra were recorded using a Bruker INVENIO-R spectrometer equipped with a liquid-nitrogen-cooled MCT detector.

COMSOL simulation of CO_2 transport Numerical simulations were performed using COMSOL Multiphysics 6.3 to investigate CO_2 transport through porous architectures. Gas transport was described using the Dusty-Gas Model (DGM), which combines Maxwell–Stefan diffusion and Knudsen diffusion and is suitable for gas transport in nanoporous media operating within the transition diffusion regime.

Two-dimensional computational domains (10 μm × 11 μm) were constructed to represent an ordered vertical-channel architecture and a disordered porous network. Both structures possessed identical porosity (0.4), average pore diameter (100 nm), and diffusion distance (10 μm) to isolate the effect of pore morphology on gas transport. Simulations were conducted for both pure CO_2 and a mixed gas composition containing 15% CO_2 and 85% N_2.

Effective diffusivities in porous domains were corrected using the Millington–Quirk model. Transient diffusion simulations were performed using the Transport of Concentrated Species interface from 0 to 2 μs. The inlet boundary was defined by a prescribed gas composition, while the outlet boundary was maintained under open diffusion conditions. The outlet CO_2 concentration was monitored to evaluate the transport performance of different porous architectures. Additional details regarding governing equations, parameter selection, geometry construction, and numerical implementation are provided in Supplementary Note 1.

Measurement of apparent CO_2 diffusion rate The apparent CO_2 diffusion behavior of gas diffusion layers was evaluated using a custom-built gas transport analysis system integrating a gas diffusion flow-cell reactor with differential electrochemical mass spectrometry (DEMS, QMG 100). The temporal response of the CO_2 signal after gas introduction was monitored in real time, and the apparent diffusion rate was quantified from the slope of the CO_2 signal evolution. Comparative measurements were conducted using the Cu-NW GDL and a commercial SGL-28 BC GDL under both pure CO_2 and 15% CO_2/N_2 feed conditions. Detailed descriptions of the experimental setup, measurement procedure, and data analysis are provided in Supplementary Note 2.

Molecular dynamics simulations To elucidate the role of nanochannel wall chemistry in confined CO_2 transport and interfacial enrichment, channel–substrate coupled molecular dynamics models were established using classical molecular dynamics simulations. Each model consisted of a Zn(100) substrate, a slit-type nanochannel, and an upper CO_2/N_2 gas reservoir. Two nanochannels with identical geometries but different wall materials (Cu(111) and graphene) were constructed to isolate the intrinsic effect of wall chemistry on confined gas transport.

All simulations were performed using the COMPASS III all-atom force field under the canonical (NVT) ensemble at 298 K with the Nosé–Hoover thermostat.[57-59] Periodic boundary conditions were applied in the X and Y directions, whereas the Z direction contained a vacuum region to eliminate interactions between periodic images. Before production runs, all systems were subjected to energy minimization followed by annealing relaxation. Production simulations were then carried out to analyze molecular diffusion trajectories, spatial concentration distributions, and interfacial CO_2 enrichment near the Zn surface. Detailed model construction, simulation parameters, and trajectory analyses are provided in Supplementary Notes 3−6.

Measurement of pH on the catalyst surface The local pH near the catalyst surface was determined using an IrO_x-modified rotating ring–disk electrode (RRDE) technique.[33, 34] The preparation of the IrO_x-modified ring electrode is described in Supplementary Note 7. IrO_x deposited on the ring electrode served as a pH-sensitive probe, and the local pH was quantified from the open-circuit potential of the ring electrode based on a pre-established calibration relationship. The pH at the catalyst-loaded disk electrode was subsequently calculated using the RRDE collection efficiency model. To reproduce the actual Zn electrodeposition interface, a Cu-NW gas diffusion layer was mounted onto the disk electrode and used as the substrate for Zn deposition. Measurements were conducted in the same electrolyte employed for the preparation of Zn-leaf and Zn-shell electrodes. Detailed descriptions of the IrO_x calibration procedure, pH calculation method, and RRDE measurement protocol are provided in Supplementary Note 8.

Preparation of Cu-NW gas diffusion layer The Cu-NW gas diffusion layer (GDL) was prepared using an optimized in situ electrooxidation strategy adapted from our previous reports.[17, 35] $Cu(OH)_2$ nanowire arrays were first grown on a porous Cu substrate by electrooxidation in alkaline electrolyte and subsequently converted into metallic Cu nanowires through H_2 reduction, yielding a hierarchical porous gas diffusion architecture. Detailed synthesis procedures and characterization of the Cu-NW GDL are described in Supplementary Note 9.

Preparation of Zn-leaf and Zn-shell gas diffusion electrodes The as-prepared Cu-NW GDL was used as the substrate for Zn electrodeposition. The electrodeposition electrolyte was prepared by mixing 30 mL of 3 M ammonium sulfate ($(NH_4)_2SO_4$), 25 mL of 0.2 M zinc sulfate heptahydrate ($ZnSO_4 \cdot 7H_2O$), and 5 mL of deionized water, resulting in an electrolyte with a pH of 4.9. Electrodeposition was carried out in a three-electrode configuration at 298 K using the Cu-NW GDL (total geometric area: 10 cm^2) as the working electrode, an Ag/AgCl electrode as the reference electrode, and a Pt foil as the counter electrode. For the preparation of Zn-leaf, a current density of −100 mA cm^{-2} was applied for 90 s. For comparison, Zn-shell was prepared under identical conditions except that a lower current density of −1 mA cm^{-2} was applied for 9000 s to maintain the same total deposition charge. After deposition, the electrode was rinsed with deionized water and dried under a nitrogen stream. PFD was dissolved in fluorinated electronic liquid (FC-770) to prepare a 0.5 wt% coating solution. Subsequently, 20 μL cm^{-2} of the coating solution was uniformly drop cast onto the dried Zn-leaf and Zn-shell electrodes. After solvent evaporation under ambient conditions, the electrodes were further dried in a vacuum oven at 298 K overnight to ensure complete removal of residual fluorinated solvent. The resulting electrodes were used as gas diffusion electrodes for CO_2RR measurements.

Density functional theory calculations Density functional theory (DFT) calculations were performed using the Vienna Ab initio Simulation Package (VASP, version 6.4.3). The projector augmented-wave (PAW) method and the Perdew–Burke–Ernzerhof (PBE) functional within the generalized gradient approximation were employed to describe the electron–ion interactions and exchange–correlation effects, respectively. Van der Waals interactions were accounted for using

the DFT-D3 correction scheme, and solvent effects were incorporated through the implicit solvation model (VASPsol). The computational hydrogen electrode (CHE) model was adopted to evaluate the energetics of electrochemical proton-coupled electron transfer steps. Detailed computational parameters are provided in Supplementary Note 10.

Electrochemical CO_2 reduction measurements Electrochemical CO_2 reduction reaction (CO_2RR) measurements were conducted in a gas diffusion flow-cell reactor using a conventional three-electrode configuration with Zn-leaf or Zn-shell as the working electrode, a Pt foil as the counter electrode, and a saturated Ag/AgCl electrode as the reference electrode. Gaseous products were quantified using an online gas chromatograph, while liquid products were analyzed by ^1H NMR and HPLC. Unless otherwise specified, all potentials were converted to the reversible hydrogen electrode (RHE) scale and corrected with 85% iR compensation. Detailed descriptions of the electrochemical setup, product analysis procedures, and data processing methods are provided in Supplementary Note 12.

Product quantification and performance evaluation Faradaic efficiencies, partial current densities, formation rates, and single-pass conversion efficiencies were calculated using standard electrochemical relationships. Detailed calculation procedures and equations are provided in Supplementary Note 13.

In situ DEMS measurements In situ differential electrochemical mass spectrometry (DEMS) measurements were performed using a QMG 100 quadrupole mass spectrometer directly coupled to a gas-tight electrochemical cell. Volatile products generated during electrolysis were continuously monitored in real time through a membrane inlet interface. Measurements were conducted in CO_2-saturated electrolytes using a conventional three-electrode configuration with Zn-leaf as the working electrode. The evolution of gaseous reaction intermediates and products was tracked simultaneously with electrochemical measurements. Detailed descriptions of the DEMS cell configuration, gas handling procedures, mass spectrometer calibration, and signal analysis are provided in Supplementary Note 15.

In situ ATR-FTIR measurements In situ attenuated total reflection Fourier-transform infrared (ATR-FTIR) spectroscopy was performed using a Bruker INVENIO-R spectrometer equipped with a liquid-nitrogen-cooled MCT detector. Zn catalyst layers recovered from the Cu-NW gas diffusion electrode were deposited onto an Au-coated Si prism to construct the ATR-FTIR working electrode, followed by hydrophobic modification using PFD. The modified prism was assembled into a custom-designed gas-tight spectro-electrochemical cell with a three-electrode configuration. Measurements were conducted in 0.1 M $KHCO_3$ electrolyte saturated with either pure CO_2 or 10% CO_2/N_2. Difference spectra were obtained by subtracting the spectrum collected at open-circuit potential from those recorded under applied potentials. Detailed procedures for prism preparation, catalyst deposition, electrode fabrication, and spectral acquisition are provided in Supplementary Note 16.

Data availability

All data are available from the authors upon reasonable request.

References

1. Porosoff, M.D., Yan, B.H. & Chen, J.G.G. Catalytic reduction of CO_2 by H_2 for synthesis of CO, methanol and hydrocarbons: challenges and opportunities. *Energy Environ. Sci.* **9**, 62-73 (2016).
2. Zhou, W. et al. New horizon in C1 chemistry: breaking the selectivity limitation in transformation of syngas and hydrogenation of CO_2 into hydrocarbon chemicals and fuels. *Chem. Soc. Rev.* **48**, 3193-3228 (2019).
3. Luk, H.T., Mondelli, C., Ferré, D.C., Stewart, J.A. & Pérez-Ramírez, J. Status and prospects in higher alcohols synthesis from syngas. *Chem. Soc. Rev.* **46**, 1358-1426 (2017).
4. Hao, S.Y. et al. Improving the operational stability of electrochemical CO_2 reduction reaction via salt precipitation understanding and management. *Nat. Energy* **10**, 266-277 (2025).
5. Hao, S.Y. et al. Acid-humidified CO_2 gas input for stable electrochemical CO_2 reduction reaction. *Science* **388** (2025).
6. Wang, Q.Y. et al. Lanthanide single-atom catalysts for efficient CO_2-to-CO electroreduction. *Nat. Commun.* **16** (2025).
7. She, X.J. et al. Kilowatt-scale alkali-cation-free CO_2 electrolysis via accelerating mass transfer. *Nat. Commun.* **17** (2026).
8. Songolzadeh, M., Soleimani, M., Takht Ravanchi, M. & Songolzadeh, R. Carbon dioxide separation from flue gases: a technological review emphasizing reduction in greenhouse gas emissions. *Sci. World J.* **2014**, 828131 (2014).
9. Zhao, Z.H. et al. Efficient Capture and Electroreduction of Dilute CO_2 into Highly Pure and Concentrated Formic Acid Aqueous Solution. *J. Am. Chem. Soc.* **146**, 14349-14356 (2024).
10. Baker, R.W., Freeman, B., Kniep, J., Huang, Y.I. & Merkel, T.C. CO_2 capture from cement plants and steel mills using membranes. *Ind. Eng. Chem. Res.* **57**, 15963-15970 (2018).
11. Chen, J. et al. Nutrient diffusion-inspired catalysts with self-reinforced concentration gradient for sustainable electroreduction of dilute CO_2. *Nat. Commun.* **16**, 7598 (2025).
12. Welch, A.J., Dunn, E., DuChene, J.S. & Atwater, H.A. Bicarbonate or carbonate processes for coupling carbon dioxide capture and electrochemical conversion. *ACS Energy Lett.* **5**, 940-945 (2020).
13. Keith, D.W., Holmes, G., Angelo, D.S. & Heidel, K. A process for capturing CO_2 from the atmosphere. *Joule* **2**, 1573-1594 (2018).
14. Seong, H. et al. Transplanting Gold Active Sites into Non-Precious-Metal Nanoclusters for Efficient CO_2-to-CO Electroreduction. *J. Am. Chem. Soc.* **145**, 2152-2160 (2023).
15. Ko, Y.J. et al. Extrinsic hydrophobicity-controlled silver nanoparticles as efficient and stable catalysts for CO_2 electrolysis. *Nat. Commun.* **15** (2024).
16. Zhou, Y.Z. et al. Asymmetric dinitrogen-coordinated nickel single-atomic sites for efficient CO_2 electroreduction. *Nat. Commun.* **14** (2023).
17. Sun, M., Cheng, J. & Yamauchi, M. Gas diffusion enhanced electrode with ultrathin superhydrophobic macropore structure for acidic CO_2 electroreduction. *Nat. Commun.* **15**, 491 (2024).
18. Xie, L.Y.Q. et al. Direct low concentration CO_2 electroreduction to multicarbon products via rate-determining step tuning. *Nat. Commun.* **15** (2024).
19. Chen, J. et al. Nutrient diffusion-inspired catalysts with self-reinforced concentration gradient for sustainable electroreduction of dilute CO_2. *Nat. Commun.* **16**, 7598 (2025).

20. Cheng, Y., Hou, P., Wang, X. & Kang, P. CO_2 electrolysis system under industrially relevant conditions. *Acc. Chem. Res.* **55**, 231-240 (2022).
21. Chen, B.Y. et al. Molecular Enhancement of Direct Electrolysis of Dilute CO_2. *Acs Energy Lett.* **9**, 911-918 (2024).
22. Nguyen, M.T., Heldebrant, D.J., Liu, J., Bhown, A.S. & Xu, Z.J. Direction-specific enhanced diffusion of CO_2 in chiral hexagonal boron nitride nanotubes. *Nat. Commun.* **17** (2026).
23. Ayres, E., van der Wal, R., Sommerkorn, M. & Bardgett, R.D. Direct uptake of soil nitrogen by mosses. *Biol. Lett.* **2**, 286-288 (2006).
24. Kanno, S. et al. Rhizoid-mediated phosphate uptake and internal transport in the non-vascular plant Marchantia polymorpha. *New Phytol.* **250**, 708-716 (2026).
25. Liu, X. et al. Zinc Hollow-Fiber Penetration Electrode Promotes Ampere-Level CO_2 Electroreduction for Viable Applications. *ACS Catal.* **15**, 4259-4269 (2025).
26. Won, D.H. et al. Highly Efficient, Selective, and Stable CO_2 Electroreduction on a Hexagonal Zn Catalyst. *Angew. Chem. Int. Ed.* **55**, 9297-9300 (2016).
27. Liu, K., Wang, J., Shi, M., Yan, J. & Jiang, Q. Simultaneous achieving of high faradaic efficiency and CO partial current density for CO_2 reduction via robust, noble-metal-free Zn nanosheets with favorable adsorption energy. *Adv. Energy Mater.* **9**, 1900276 (2019).
28. Wan, L. et al. Bimetallic Cu-Zn Catalysts for Electrochemical CO_2 Reduction: Phase-Separated versus Core-Shell Distribution. *ACS Catal.* **12**, 2741-2748 (2022).
29. Luo, W., Zhang, J., Li, M. & Zuttel, A. Boosting CO Production in Electrocatalytic CO_2 Reduction on Highly Porous Zn Catalysts. *ACS Catal.* **9**, 3783-3791 (2019).
30. Rosen, J. et al. Electrodeposited Zn Dendrites with Enhanced CO Selectivity for Electrocatalytic CO_2 Reduction. *ACS Catal.* **5**, 4586-4591 (2015).
31. Sun, M., Staykov, A. & Yamauchi, M. Understanding the Roles of Hydroxide in CO_2 Electroreduction on a Cu Electrode for Achieving Variable Selectivity. *ACS Catal.* **12**, 14856-14863 (2022).
32. Sun, M., Cheng, J., Anzai, A., Kobayashi, H. & Yamauchi, M. Modulating Electronic States of Cu in Metal-Organic Frameworks for Emerging Controllable CH_4/C_2H_4 Selectivity in CO_2 Electroreduction. *Adv. Sci.* **11**, 2404931 (2024).
33. Guo, J. et al. Direct seawater electrolysis by adjusting the local reaction environment of a catalyst. *Nat. Energy* (2023).
34. Yokoyama, Y. et al. In Situ Local pH Measurements with Hydrated Iridium Oxide Ring Electrodes in Neutral pH Aqueous Solutions. *Chem. Lett.* **49**, 195-198 (2020).
35. Sun, M. et al. In Situ Observation of Post-CO Intermediates to Decode C─C Coupling Pathways in CO_2 Electroreduction. *Angew. Chem. Int. Ed.*, e202502740 (2025).
36. Wöll, C. The chemistry and physics of zinc oxide surfaces. *Prog. Surf. Sci.* **82**, 55-120 (2007).
37. Coppa, B. et al. In situ cleaning and characterization of oxygen-and zinc-terminated, n-type, ZnO {0001} surfaces. *J. Appl. Phys.* **95**, 5856-5864 (2004).
38. Gupta, D., Mao, J. & Guo, Z. Bifunctional catalysts for CO_2 reduction and O_2 evolution: a pivotal for aqueous rechargeable Zn− CO_2 batteries. *Adv. Mater.* **36**, 2407099 (2024).
39. Wakerley, D. et al. Gas diffusion electrodes, reactor designs and key metrics of low-temperature CO_2 electrolysers. *Nat. Energy* **7**, 130-143 (2022).
40. Lees, E.W., Mowbray, B.A.W., Parlane, F.G.L. & Berlinguette, C.P. Gas diffusion electrodes and membranes for CO_2 reduction electrolysers. *Nat. Rev. Mater.* **7**, 55-64 (2021).

41. Hao, Q. et al. Universal Formation of Single Atoms from Molten Salt for Facilitating Selective CO_2 Reduction. *Adv. Mater.* **36**, e2406380 (2024).
42. Chen, J. et al. Promoting Hydrogen Transfer in Electrochemical CO_2 Reduction via a Hydrogen on Demand Pathway. *Angew. Chem. Int. Ed.* **64**, e202422775 (2025).
43. Wei, S. et al. Planar chlorination engineering induced symmetry-broken single-atom site catalyst for enhanced CO_2 electroreduction. *Nat. Commun.* **16**, 1652 (2025).
44. Zhang, Z. et al. Selective and Scalable CO_2 Electrolysis Enabled by Conductive Zinc Ion-Implanted Zeolite-Supported Cadmium Oxide Nanoclusters. *J. Am. Chem. Soc.* **146**, 6397-6407 (2024).
45. Papangelakis, P. et al. Improving the SO_2 tolerance of CO_2 reduction electrocatalysts using a polymer/catalyst/ionomer heterojunction design. *Nat. Energy* **9**, 1011-1020 (2024).
46. Zhu, H.-J. et al. Oxygen-tolerant CO_2 electroreduction over covalent organic frameworks via photoswitching control oxygen passivation strategy. *Nat. Commun.* **15**, 1479 (2024).
47. Ko, B.H. et al. The impact of nitrogen oxides on electrochemical carbon dioxide reduction. *Nat. Commun.* **11**, 5856 (2020).
48. Kibria, M.G. et al. Electrochemical CO_2 reduction into chemical feedstocks: from mechanistic electrocatalysis models to system design. *Adv. Mater.* **31**, 1807166 (2019).
49. O'Brien, C.P. et al. CO_2 electrolyzers. *Chem. Rev.* **124**, 3648-3693 (2024).
50. Lv, K. et al. Hydrophobic and electronic properties of the E-MoS_2 nanosheets induced by FAS for the CO_2 electroreduction to syngas with a wide range of CO/H_2 ratios. *Adv. Funct. Mater.* **28**, 1802339 (2018).
51. Li, F. et al. Electrosynthesis of ethylene from syngas. *Nat. Sustain.* **9**, 585-594 (2026).
52. Firet, N.J. & Smith, W.A. Probing the Reaction Mechanism of CO_2 Electroreduction over Ag Films via Operando Infrared Spectroscopy. *ACS Catal.* **7**, 606-612 (2017).
53. Yang, Y. et al. Decoupling Product Selectivity in Electrocatalytic CO_2 Reduction by Steering the Interfacial Water Structure. *J. Am. Chem. Soc.* **148**, 11284-11295 (2026).
54. Wang, Y. et al. Strong Hydrogen-Bonded Interfacial Water Inhibiting Hydrogen Evolution Kinetics to Promote Electrochemical CO_2 Reduction to C_{2+}. *ACS Catal.* **14**, 3457-3465 (2024).
55. Li, L. & Cui, C. Bulk water redox chemistry enables radical-mediated C-C coupling in CO_2 electroreduction. *Nat. Chem.* (2025).
56. Zhang, H., Raciti, D. & Hall, A.S. Disordered interfacial H_2O promotes electrochemical C-C coupling. *Nat. Chem.* (2025).
57. Akkermans, R.L., Spenley, N.A. & Robertson, S.H. COMPASS III: automated fitting workflows and extension to ionic liquids. *Mol. Simul.* **47**, 540-551 (2021).
58. Yang, J., Ren, Y., Tian, A.-m. & Sun, H. COMPASS force field for 14 inorganic molecules, He, Ne, Ar, Kr, Xe, H_2, O_2, N_2, NO, CO, CO_2, NO_2, CS_2, and SO_2, in liquid phases. *J. Phys. Chem. B* **104**, 4951-4957 (2000).
59. Evans, D.J. & Holian, B. The nose–hoover thermostat. *A)'=(A Is)* **1**, 18 (1985).

Acknowledgments

We acknowledge funding from Natural Science Foundation for Young Scholars of Jiangsu Province (No. BK20241422), National Natural Science Foundation of China (No. 22479075), the supporting funds for talents of Nanjing University of Aeronautics and Astronautics. We thank the Center for Microscopy and Analysis at Nanjing University of Aeronautics and Astronautics for the assistance of the characterization support.

Author contributions

Conceptualization: M.S. Methodology: M.S. Investigation: M.S., Y.W, and Z.T. Visualization: M.S. Funding acquisition: M.S., and Y.Z. Project administration: M.S. Supervision: M.S., and Y.Z. Writing – original draft: M.S. Writing – review & editing: M.S., and Y.Z.

Competing interests

Authors declare that they have no competing interests.

Materials & Correspondence

Materials & Correspondence should be addressed to Yinlong Zhu.

Supplementary Files

This is a list of supplementary files associated with this preprint. Click to download.

- NatCommunSIf.docx